Journal of Atmospheric and Solar-Terrestrial Physics 127 (2015) 21–29

Contents lists available at ScienceDirect

Journal of Atmospheric and Solar-Terrestrial Physics

journal homepage: www.elsevier.com/locate/jastp

The seasonal cycle of gravity wave momentum flux and forcing in the high latitude northern hemisphere mesopause region

R.J. de Wit [a,*], R.E. Hibbins [a,b], P.J. Espy [a,b]

[a] Norwegian University of Science and Technology (NTNU), Trondheim, Norway
[b] Birkeland Centre for Space Science, Bergen, Norway

ARTICLE INFO

Article history:
Received 18 June 2014
Received in revised form
24 September 2014
Accepted 6 October 2014
Available online 13 October 2014

Keywords:
Meteor radar
Gravity wave
Gravity wave momentum flux
MLT
Middle atmosphere dynamics
Vertical coupling

ABSTRACT

A new generation all-sky SKiYMET meteor radar, optimized to measure high-frequency gravity wave momentum flux, was installed in Trondheim, Norway (63.4°N, 10.5°E), and has been providing near-continuous measurements since September 2012. Using the system's first full calendar year of observations the seasonal cycle of gravity wave momentum flux and forcing in the mesopause region is studied. The vertical flux of zonal momentum is observed to change from westward to eastward with increasing altitude in winter, and from eastward to westward in summer. This vertical divergence results in westward gravity wave forcing in winter, and eastward forcing in summer. It is shown that the seasonal cycle in gravity wave momentum flux and forcing can be interpreted in terms of selective filtering of a uniform spectrum of vertically propagating GWs between the surface and the mesopause region.

1. Introduction

It is widely acknowledged that gravity waves (GWs) are not solely an interesting atmospheric phenomenon, but play an important role in atmospheric dynamics due to their ability to redistribute energy and couple different atmospheric layers (e.g. Nappo, 2002; Fritts and Alexander, 2003). Indeed, GWs are understood to be the main driver of the general circulation in the quiescent mesosphere/lower thermosphere (MLT) (e.g. Holton, 1983; Fritts and Alexander, 2003 and references therein). GWs propagating upward from the lower atmosphere encounter selective filtering in the stratospheric winds (Lindzen, 1981), which in turn determines the GW spectrum and its corresponding momentum flux reaching the MLT. This process plays an important role in establishing the summer to winter pole circulation in the MLT, thus driving the MLT away from radiative equilibrium (e.g. Holton, 1983; Vincent, 2009).

Due to their relatively small scales, GWs are generally not resolved in global circulation and climate models, but rather their effects are parameterized in order to produce realistic wind and temperature fields (Geller et al., 2013), although it must be noted that high resolution models capable of explicitly resolving an increasing portion of GW scales are now becoming available (e.g. Becker, 2009). A key parameter to guide and constrain these parameterizations is the GW momentum flux, and in particular knowledge of its seasonal and latitudinal variation is important (Espy et al., 2006; Geller et al., 2013). Different methods have been used to study GWs in the MLT. One such method is the use of satellite instruments like Sounding of the Atmosphere using Broadband Emission Radiometry (SABER) to measure GW momentum flux (e.g. Ern et al., 2011), where GW amplitudes are derived from measured temperature profiles. The major advantage of this technique is that it provides global scale coverage and provides information regarding latitudinal variations, albeit for a limited range of GW temporal and spatial scales. However, no directional information about the GW momentum flux can be obtained using this method. Directional GW momentum flux in the MLT region can be derived using various other techniques, including combined radar and airglow observations (e.g. Gardner et al., 1999; Espy et al., 2004, 2006), and studies using dual-beam radars (e.g. Vincent and Reid, 1983; Fritts and Vincent, 1987; Janches et al., 2006; Fritts et al., 2006).

A generalization of the dual-beam method (Vincent and Reid, 1983) was proposed by Hocking (2005), enabling GW momentum flux observations in the MLT using meteor radar measurements, and is based on the notion that fluctuations in the wind field, after removal of a background wind, represent the true wind variability due to GWs (Hocking, 2005). The technique has been used to study momentum fluxes using standard meteor radars (Hocking et al., 2001) at high latitude (Hocking, 2005; Placke et al., 2011a), mid-latitude (Hocking, 2005; Placke et al., 2011a, 2011b), and tropical

* Corresponding author.
E-mail address: rosmarie.wit@ntnu.no (R.J. de Wit).

http://dx.doi.org/10.1016/j.jastp.2014.10.002
1364-6826/

sites (Antonita et al., 2008). Due to the relatively large network of meteor radars (Hocking, 2005) as well as their capability to obtain continuous measurements, meteor radars appear to be well suited to study latitudinal variation as well as the seasonal cycle of the GW momentum flux.

A limiting factor in the determination of GW momentum fluxes using meteor radars is the meteor count rate and zenith angle distribution (Hocking, 2005, 2011; Andrioli et al., 2013). When meteor counts are low, the use of long averaging time intervals on the order of one month is necessary, compromising the temporal resolution with which the GW momentum flux variability can be derived. In order to optimize meteor radars to determine GW momentum fluxes, a new generation SKiYMET system was developed and first deployed on Tierra del Fuego (53.8°S, 67.8°W) (Fritts et al., 2010a,b). Here, 8 transmitter antennas are combined in order to achieve high peak powers and to direct most of this power in the area between 15° and 50° zenith angle, resulting in high meteor count rates in the region of interest for the determination of GW momentum fluxes (Fritts et al., 2010a,b). Indeed, using the meteor distribution detected with the optimized system, Fritts et al. (2010a) showed that GW momentum flux estimates remain reliable when averaging time scales were reduced to as low as 10 days.

The first northern hemisphere SKiYMET meteor radar optimized to measure GW momentum fluxes is located in Trondheim, Norway (63.4°N, 10.5°E), and has been operational since September 2012. This study presents the first observations of the seasonal cycle of GW momentum flux and forcing during 2013 obtained with this new generation radar. The system design and data analysis techniques are described in Section 2. As meteor statistics are an important factor when determining GW momentum fluxes, meteor statistics over 2013 are presented in Section 3. Afterwards, the seasonal cycle in the horizontal winds and the high-frequency GW momentum flux and forcing are presented. In Section 4, the GW momentum flux and forcing are discussed in light of previous observations as well as the background wind field.

2. System specifications and data analysis

2.1. System specifications

The Trondheim Meteor Radar is an all-sky SKiYMET meteor radar (Hocking et al., 2001) located in Trondheim, Norway (63.4°N, 10.5°E) and has been operating near-continuously since September 2012. The system is similar in design to the SAAMER and DrAAMER radars (Fritts et al., 2010a,b, 2012), and is optimized to measure GW momentum fluxes in addition to traditional meteor radar parameters such as horizontal winds and temperatures. To this end, the transmitter array consists of 8 three-element Yagi antennas in a circular orientation, supplying a peak power of 30 kW. During normal operation most of the power is directed into eight beams at 45° azimuth increments, with peak powers around 35° off-zenith and a majority of meteors detected between 15° and 50° zenith angle (see e.g. Fritts et al., 2010b, their Fig. 1). Other transmitter phasings are also possible, allowing for different beam-modes. One of the set-ups available is a vertical beam-mode, in which the radar ran for 2 consecutive days in July 2013 (9.58 UT 10/7–11.42 UT 12/7) without any detrimental effect on routine observations.

The return signal is detected on 5 three-element Yagi antennas, spaced at 2λ and 2.5λ, increasing detection precision. Details on receiver antenna layout, and routine meteor positioning and radial velocity determination can be found in Hocking et al. (2001).

The radar frequency of 34.21 MHz is optimized for meteor detection at peak meteor ablation altitudes. Peak count rates are observed around 90 km, and generally enough meteors are detected in the range of 70–100 km for the derivation of horizontal winds throughout this region (see also Section 3.1). A pulse repetition frequency of 925 Hz and a pulse width of 2 km were used throughout 2013.

Data coverage for 2013 was 96%, with brief periods of downtime due to maintenance and system failure. Data gaps of more than 24 h are present from 05/03 (12 UT) to 05/04 (18 UT), 07/24 (0 UT) to 07/26 (14 UT), 08/04 (13 UT) to 08/05 (12 UT), 08/10 (18 UT) to 08/13 (12 UT), and 08/23 (20 UT) to 08/27 (12 UT). Between 05/26 and 06/07 a power amplifier problem caused a slightly distorted beam pattern and a 25% reduction in transmitter power.

2.2. Data analysis

Horizontal winds between 70 and 100 km are determined for 60-min time intervals and several altitude intervals by performing a least-squares best fit to the measured radial velocities when at least 7 meteors are present in the altitude interval (Hocking et al., 2001). The altitude intervals used are 8 km (70–78 km), 4 km (78–82 km), 2 km (82–96 km), and again 4 km (96–100 km) to correct for the change of meteor count rates with altitude. In the horizontal wind determination, as well as all other analysis described in this study, only unambiguously detected meteors between 15° and 50° zenith angle have been used. In addition to the horizontal wind, the mean meteor time and height (defined as the average meteor detection time and altitude) are determined for each individual time–height interval. These parameters reflect the non-uniform distribution of meteors in time and altitude, and using these parameters ensures that the derived horizontal winds are assigned to the altitude and point in time best representing their occurrence.

From the hourly zonal and meridional winds in each altitude interval, moving averages were created by performing a least-squares fit over a time period of 4 days (time-stepped by 1 day) using an offset representing the 4-day moving-average horizontal wind, together with oscillations with periods of 48- (representing a 2-day planetary wave), 24-, 12-, and 8-h (tides) when at least half of the data were present in the time interval.

High-frequency GW momentum fluxes were derived for four 4 km altitude intervals between 80 and 96 km in a manner similar to that described in de Wit et al. (2014). A proper removal of the background wind is crucial in order to obtain reliable momentum flux estimates (Andrioli et al., 2013), especially in regions where large amplitude high frequency tides are present, as is the case in the Scandinavian MLT (e.g. Mitchell et al., 2002). The hourly mean horizontal winds were linearly interpolated in height and time to the altitude and time of each individual meteor detection. The component of this meteor-specific background wind along the meteor's line-of-sight was subtracted off the individual meteor's observed radial velocity to derive the residual velocity perturbation due to high-frequency GWs. Then, using the matrix-inversion method proposed by Hocking (2005) 90-min momentum fluxes (45 min periods centered around the nominal time, shifted in 1-h time steps) are calculated from the velocity perturbations when at least 30 meteors are available. These hourly values are then combined in monthly (cf Fig. 4) or 10-day moving averages (cf Fig. 5). When calculating these averages and corresponding $1-\sigma$ standard errors of the mean, momentum fluxes obtained from the inversion of a near-singular matrix or with an absolute value exceeding 300 $m^2\,s^{-2}$ are discarded as, although mathematically correct, these results are considered to be non-physical (Hocking, personal communication). Using this method, momentum fluxes from high-frequency GWs with periods up to the order of 2–3 h can be derived (Hocking, 2005). Although the GW spectrum

reaching the MLT is much broader, the high-frequency end of the GW spectrum is believed to dominate the transport of momentum into the middle atmosphere (e.g. Fritts and Vincent, 1987; Reid and Vincent, 1987), suggesting that the meteor radar technique is sensitive to that part of the spectrum important for energy transport.

The vertical divergence of the momentum flux, corrected for the decrease of density with height, was used to provide an estimate of the GW forcing (GWF). 10-day moving average density weighted zonal momentum fluxes, $\rho\overline{u'w'}$, were derived for 2 altitude intervals between 80–90 and 90–100 km, using CIRA-86 monthly mean densities (Fleming et al., 1990). Using

$$GWF(z) = -\frac{1}{\rho(z)}\frac{\partial(\rho\overline{u'w'})}{\partial z} \quad (1)$$

(e.g. Reid and Vincent, 1987), the mean forcing due to high-frequency GWs at around 90 km was estimated (de Wit et al., 2014). The uncertainty in the GWF is derived by summing in quadrature the $1-\sigma$ standard errors of the mean of $\rho\overline{u'w'}$ in each of the altitude intervals. The final uncertainty is determined following regular error propagation of Eq. (1), considering all other parameters in the determination of the GWF to be without uncertainty.

3. Results

3.1. Meteor statistics

Daily meteor count rates of unambiguous meteor detections between 70 and 100 km and 15° and 50° zenith angle (from now on referred to as 'useful meteors') from January until December 2013 are shown in Fig. 1(a). Days with one or more hours of radar down time are marked with a green cross. Daily meteor counts are generally high, with notable exceptions occurring at times with significant radar downtime. Count rates are observed to peak in NH summer and to fall off in winter, in line with theoretical considerations as well as observations (Singer et al., 2004; Younger et al., 2009). From January to March, and again from November to December between about 5000 and 7000 meteors are observed per day. Count rates of about 8000 useful meteors a day and upward are found between April and October, with maximum daily useful meteor counts of up to about 12 000 in the first half of June.

Meteor count rates maximize around 90 km and fall off above and below this level, as can be seen in Fig. 1(b), which shows the altitude distribution of monthly mean meteor counts per hour per kilometer throughout the year. A seasonal cycle, with meteor count rates maximizing at higher altitudes around the equinoxes, is apparent, similar to meteor radar observations over Andenes (69°N, 16°E) (Stober et al., 2012). Stober et al. (2012) noted that it is currently unclear whether this behavior is caused by density variations or if it stems from extraterrestrial origin. Although meteor count rates are considerably lower between about 70 and 80 km as compared to the altitude of maximum meteor count rates, generally enough meteors are collected for the determination of horizontal winds. However, as can be seen in Fig. 1(b), during NH summer meteor count rates between about 70 and 75 km show a minimum, rendering the determination of horizontal winds at the lowest altitudes difficult.

Due to the large, rapidly changing tides at the altitudes and latitude under consideration, it is important that meteor count rates remain sufficiently high throughout the day to guarantee reliable wind measurements. Fig. 2(a) shows the diurnal variability

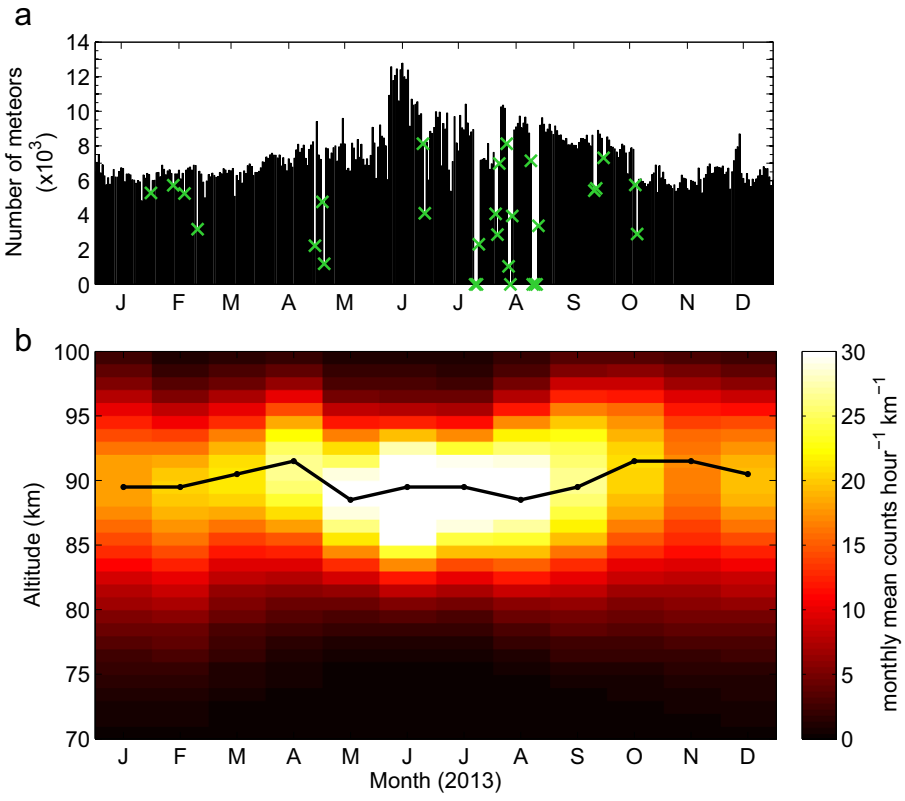

Fig. 1. (a) Daily counts of unambiguous meteor detections between 70 and 100 km and 15° and 50° zenith angle from January to December 2013 over Trondheim, Norway. Green crosses denote days for which the radar down time was one hour or more. (b) Altitude distribution of monthly mean 'useful' meteor counts per hour per km. Maximum meteor count altitudes are indicated with a black dot for each month.

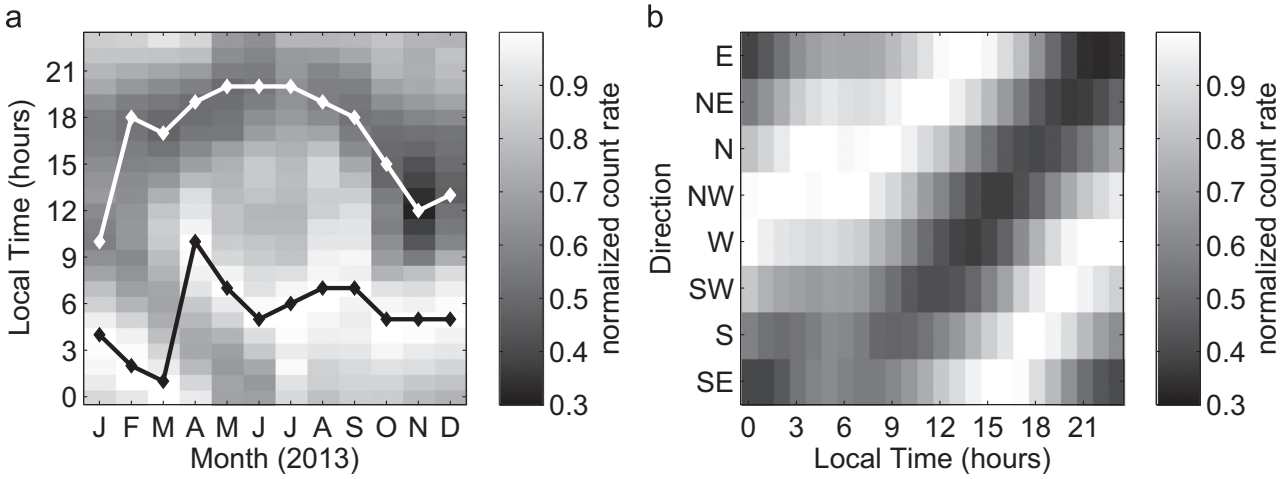

Fig. 2. (a) Diurnal variation in normalized hourly meteor count rate as a function of month (normalized to maximum count rate each month). The time of maximum (minimum) count rate is indicated with a black (white) diamond for each month. (b) Azimuthal variability of hourly meteor count rate as a function of time (normalized to maximum count rate for every hour). Azimuthal bins are taken as 180° centered symmetrically on the indicated azimuth angle. Directions range from east (top) counter-clockwise to the south–east (bottom).

of hourly meteor count rates of useful meteors throughout the year. Maximum count rates (indicated by black diamonds) are observed during the morning hours, generally occurring earlier during NH winter than during summer. From January until March 2013 the maximum count rates occur increasingly early, from 4 LT to 1 LT, after which it jumps to 10 LT in April. Maximum count rates from April to September occur on average around 7 LT, shifting to 5 LT from October to December. Minimum count rates (indicated by white diamonds in Fig. 2(a)) follow a similar cycle throughout the year as maximum count rates, with minimum count rates occurring at 10 LT in January, and occurring increasingly later in the day towards summer. Minimum count rates from May to July occur around 20 LT, and occur progressively earlier towards the end of the year, with minimum count rates occurring in December around 13 LT. The daily cycle of minimum and maximum count rates is discussed in Singer et al. (2004) and Younger et al. (2009).

Momentum flux estimates are based on the comparison of motions in two opposite halves of the sky (Vincent and Reid, 1983), hence a challenge for momentum flux determination is the diurnal variability in the azimuthal distribution of meteors (Fritts et al., 2010b). Fig. 2(b) shows a composite day (based on data recorded throughout 2013) of the azimuthal distribution of hourly meteor count rates as a function of local time, where the azimuthal bin has been taken to span 180°. Indeed, a diurnal cycle is present in the preferred direction of observed meteors, with minimum count rates occurring in the south–east in the early morning, changing clockwise over the course of 24 h. This is a concern, since the limiting factor for the determination of the momentum flux is that half of the sky with the lowest count rates, regardless of the count rates in the opposite half of the sky (e.g. Fritts et al., 2010a). However, the azimuthal modulation is small. Since the minimum count rates never fall below 30% of the maximum count rate, we anticipate the effect of the azimuthal modulation on the momentum flux determination to be small.

3.2. Horizontal winds

To study the seasonal cycle in the horizontal wind, the 4-day moving-average mean zonal and meridional winds are computed and shown in Fig. 3. Here, horizontal winds are only shown if hourly horizontal winds were available during at least 48 h out of the 4-day interval. The upper and lower altitude limits for the wind determination vary in time due to the use of the mean

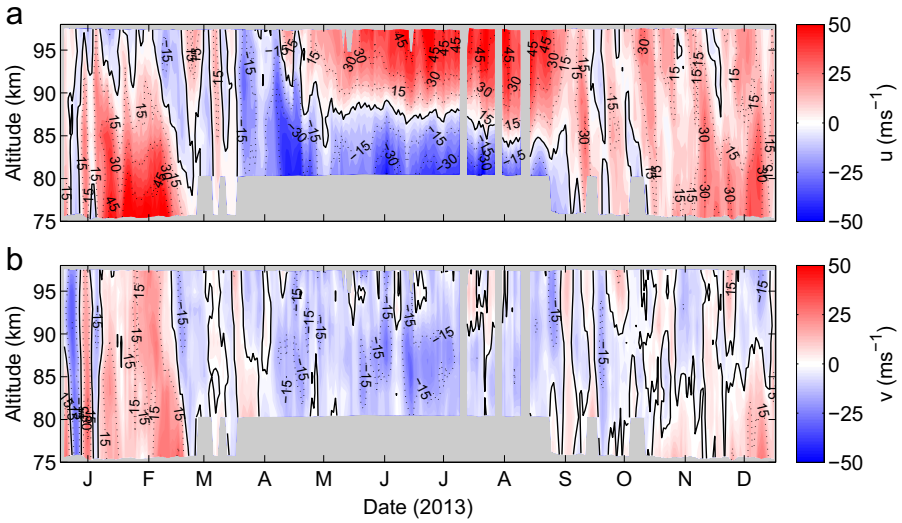

Fig. 3. 4-day moving average zonal wind (a) and meridional wind (b) (in m s^{-1}) as a function of altitude for 2013. Gray indicates lacking data.

meteor height, in which for each time-height interval the representative height in terms of meteor detections is determined. Furthermore, the 3 periods of radar down time can be observed in July and August. Another feature that stands out is the lack of data in the lowest altitude bin from 70 to 78 km in summer. This reflects the reduced meteor count rates at these altitudes during summer, as seen in Fig. 1 and discussed earlier.

The 4-day moving-average mean zonal wind (Fig. 3(a)) is generally eastward throughout January and February, with some periods of westward winds mainly occurring above 90 km. The westward winds extending from 75 to 100 km in early January are associated with a major Sudden Stratospheric Warming (SSW). A full discussion of the observed effect of the major SSW on the MLT zonal wind, GW momentum flux and GW forcing over Trondheim can be found in de Wit et al. (2014). In March winds are alternating eastward and westward throughout the observed column, and turn westward in April. Towards the end of April, a zero-wind line with eastward winds above and westward winds below starts to descend from ~98 km. By mid-May the zero-wind line can be seen to have reached an altitude between 85 and 90 km, where it remains until the beginning of August. During this time eastward winds in excess of 45 m s^{-1} can be observed at the upper levels, and westward winds in excess of -30 m s^{-1} at the lower levels. From the beginning of August until mid-September the zero-wind line descends further to about 75 km. From this time onwards, the zonal wind is generally eastward throughout the observed height range.

Comparing the 4-day moving-average mean meridional wind (Fig. 3(b)) to the zonal wind, it is clear that meridional winds are weaker than zonal winds and are generally more variable. February is characterized by northward winds at all altitudes under consideration, whereas from May to August southward winds prevail. During all other months northward and southward winds alternate, indicating the presence of planetary waves (PWs) throughout most of autumn and winter (e.g. Pancheva and Mitchell, 2004; Kleinknecht et al., 2014). A particularly clear example of PW activity can be seen throughout January, in relation to the major SSW (de Wit et al., 2014).

The zonal winds observed over Trondheim agree well with climatological conditions in the Scandinavian mesopause region. A 10-year climatology of monthly mean winds over Esrange derived using meteor radar observations (Sandford et al., 2010) reveals zonal winds between ± 50 m s^{-1}, the same range as found over Trondheim. Also the seasonal cycle in mesopause zonal winds over Trondheim is in agreement with climatological conditions, which show generally weak eastward winds throughout winter, and stronger eastward winds in April. After this, the zero-wind line descends, creating a region of eastward winds overlying westward winds during summer. Similarly, the monthly mean meridional winds reported in Sandford et al. (2010) reach maxima of ± 20 m s^{-1}, again weaker than the zonal winds, and in the same range as the meridional winds observed over Trondheim. Although the general behavior of the meridional winds over Esrange is similar to that over Trondheim, the Trondheim 4-day moving-average meridional winds have higher variability than the zonal winds due to PWs, making it more difficult to compare them with the monthly mean values presented for Esrange.

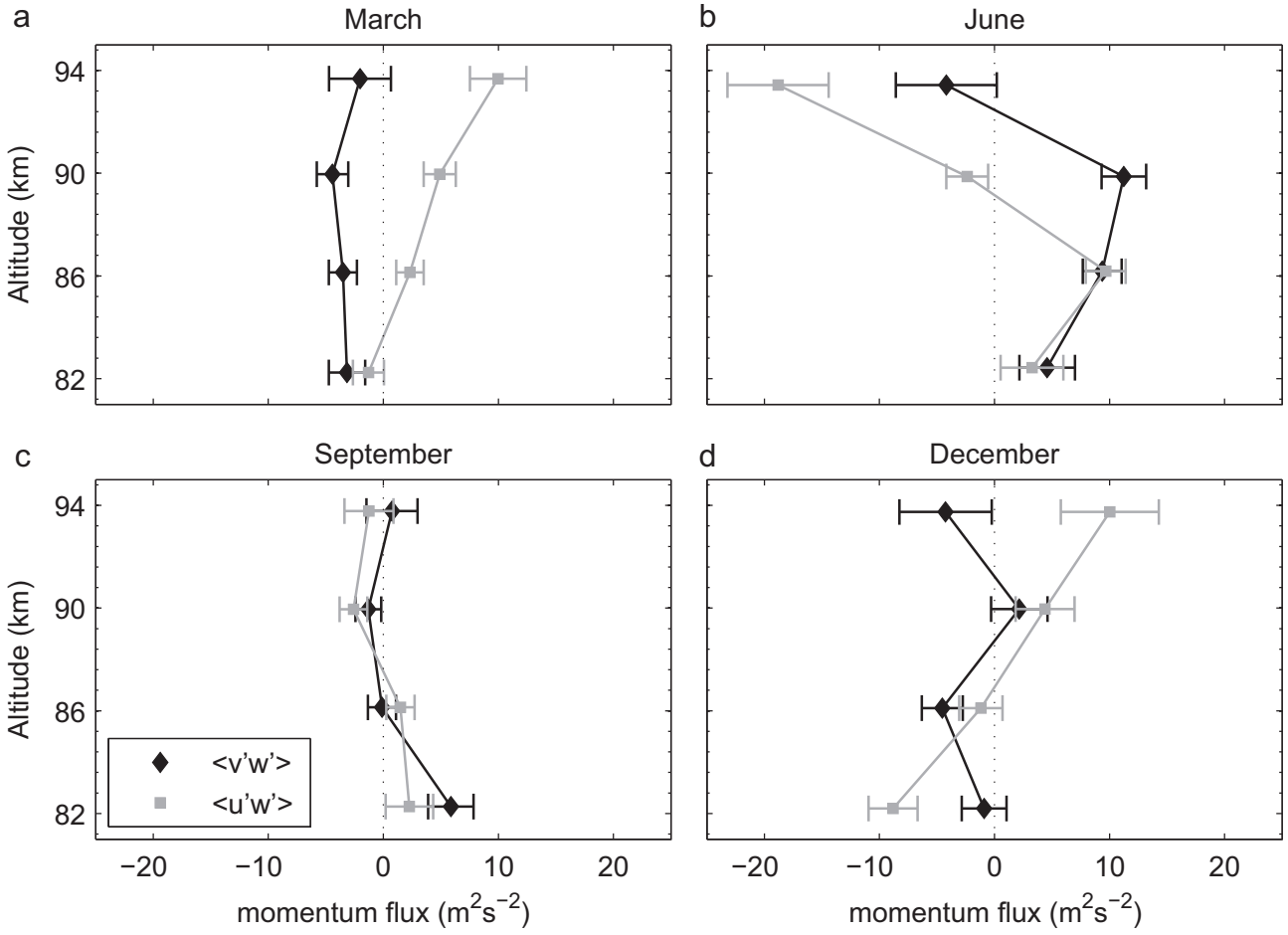

Fig. 4. Monthly average GW momentum flux $\overline{u'w'}$ (gray squares) and $\overline{v'w'}$ (black diamonds) (in m^2 s^{-2}) for (a) March, (b) June, (c) September, and (d) December. Error bars indicate the $1-\sigma$ standard error of the mean.

3.3. High-frequency GW momentum flux

In Fig. 4, the monthly mean zonal and meridional momentum fluxes are presented for March, June, September and December, as approximations for solstice and equinox conditions. Monthly mean values of $\overline{v'w'}$ for these months typically lie between $\pm 10\ m^2\ s^{-2}$. In March, $\overline{v'w'}$ can be seen to be weakly equatorward with values below $5\ m^2\ s^{-2}$. In June, below 92 km, $\overline{v'w'}$ is poleward, with a maximum value of $11.3 \pm 2.0\ m^2\ s^{-2}$. While at 93.4 km $\overline{v'w'}$ turns equatorward, it should be noted that this value is not statistically significantly different from zero. Similarly, in September $\overline{v'w'}$ is not significantly different from zero, except at 82.3 km where $\overline{v'w'}$ is poleward ($5.9 \pm 2.0\ m^2\ s^{-2}$). For December a mixed picture arises, with statistically significant equatorward GW momentum fluxes derived for the 86.1 km and 93.7 km levels.

In contrast, somewhat larger values are found for $\overline{u'w'}$, which range between $-18.8 \pm 4.4\ m^2\ s^{-2}$ and $+10.0 \pm 4.3\ m^2\ s^{-2}$. In March, $\overline{u'w'}$ slopes from weak westward to eastward with increasing height, whereas in June $\overline{u'w'}$ changes from eastward below 88 km to $-18.8 \pm 4.4\ m^2\ s^{-2}$ at the top level. During September $\overline{u'w'}$ is generally around zero. Throughout December $\overline{u'w'}$ again slopes from westward ($-8.8 \pm 2.1\ m^2\ s^{-2}$ at 82.2 km) to eastward ($10.0 \pm 4.3\ m^2\ s^{-2}$ at 93.7 km). These results are discussed in more detail in the next section.

4. Discussion

The range of zonal and meridional GW momentum fluxes observed over Trondheim from $\sim -20\ m^2\ s^{-2}$ to $\sim +10\ m^2\ s^{-2}$ is within the range previously derived from meteor radar measurements. In the European sector, 28-day average zonal and meridional GW momentum fluxes in the range of $\pm 12\ m^2\ s^{-2}$ were reported for the Scandinavian high-latitude site Andenes (69.3°N, 16.0°) and the mid-latitude site Juliusruh (54.6°N, 13.4°E) (Placke et al., 2011a), while for Collm (51.3°N, 13.0°E) reported values are slightly higher with maxima of up to $\pm 15\ m^2\ s^{-2}$ (Placke et al., 2011b). Hocking (2005) reported 2-monthly mean values of $\overline{u'w'}$ never exceeding $\pm 20\ m^2\ s^{-2}$ over Resolute Bay (75°N, 95°W), and within $\pm 10\ m^2\ s^{-2}$ over Socorro (34°N, 107°W). At low latitudes (Trivandrum, 8.5°N, 76.9°E), Antonita et al. (2008) reported daily mean values for a typical day in April 2007 between $\sim -30\ m^2\ s^{-2}$ and $\sim +10\ m^2\ s^{-2}$ for $\overline{u'w'}$, as well as monthly means within $\pm 10\ m^2\ s^{-2}$ for both $\overline{u'w'}$ and $\overline{v'w'}$. Finally, using a system similar in design to the meteor radar used in the present study, Fritts et al. (2010a) found monthly mean $\overline{u'w'}$ in the range of $\pm 20\ m^2\ s^{-2}$ over Tierra del Fuego (53.8°S, 67.8°W). Higher values were found to coincide with times when a stratospheric GW hotspot was present (Fritts et al., 2010a).

Combined radar and Na airglow imager observations of GW momentum fluxes over Halley (76°S, 27°W) show mean wintertime values of $-7.5\ m^2\ s^{-2}$ for $\overline{u'w'}$, and $1.6\ m^2\ s^{-2}$ for $\overline{v'w'}$ in an 8 km layer centered at around 90 km, while values over the mountainous sites of Rothera (67°S, 68°W) were about 4 times larger (Espy et al., 2004, 2006). Tang et al. (2002) reported winter (summer) time values $\overline{u'w'}$ and $\overline{v'w'}$ of -19.79 (-2.37) $m^2\ s^{-2}$, and -11.95 (13.70) $m^2\ s^{-2}$, respectively, in the OH airglow layer at a mountainous site at 35°N, 107°W. The larger GW momentum flux values over the two mountainous sites as compared to Halley were attributed to differences in GW source functions (Espy et al., 2006).

While the order of magnitude of GW momentum flux observed over Trondheim is in agreement with these airglow observations, the GW propagation directions are different for the different sites. Although this can indicate a genuine geophysical effect, it can be seen from Fig. 4 that vertical gradients in the GW momentum fluxes are present, leading in some months to a sign change within the 80–96 km observation interval. Hence, small changes in observation altitude as well as coarse vertical resolution can lead to differences in observed GW propagation direction, making a comparison difficult.

Comparing the vertical gradients in GW momentum flux displayed in Fig. 4 to the two-monthly mean values of zonal GW momentum flux from three-year climatologies at Resolute Bay and Socorro (Hocking, 2005), it can be seen that not only the range of $\overline{u'w'}$, but also the observed seasonal cycle agree well. During June (Fig. 4(b)), eastward $\overline{u'w'}$ turns westward with increasing altitude, whereas during December (Fig. 4(d)) the opposite is true, in agreement with the slope in $\overline{u'w'}$ presented in Hocking (2005). During March (Fig. 4(a)) an eastward tilt with increasing altitude is observed, as in December, although the vertical divergence is smaller during March than during December. It should be noted that Hocking (2005) reported a negative (Socorro) or no clear (Resolute Bay) slope during the March–April interval. However, this could be due to the inclusion of April, during which more summer-like (and hence a negative slope) conditions could be expected. In September (Fig. 4(c)) no clear slope is seen, which is again in agreement with Hocking (2005).

From the comparison with previous meteor radar and airglow studies, it appears that results from the Trondheim meteor radar are consistent with other GW momentum flux observations from mid-to-high latitudes on monthly time scales. However, it was shown that for the meteor distributions obtained with the SAAMER system, the time resolution for which meaningful GW momentum fluxes could be derived could successfully be reduced to 10 day averages (Fritts et al., 2010b). As the current radar is similar in design to this system, the zonal GW momentum flux analysis was repeated using a 10-day moving average to study the temporal variability of $\overline{u'w'}$ in more detail (Fig. 5(a)). It is clear that the zonal GW momentum flux observed here exhibits a high temporal variability, as has previously been reported by e.g. Fritts and Vincent (1987), Hocking (2005) and Espy et al. (2006), although a seasonal pattern can be discerned here as well. Generally, $\overline{u'w'}$ tilts positive with increasing height during winter, when $\overline{u'w'}$ is seen to be westward at the lower levels and to turn eastward at the upper levels. The opposite is true in summer, when $\overline{u'w'}$ is eastward below and turns westward with height, reaching minimum values of $-30\ m^2\ s^{-2}$ at 96 km.

This is an interesting notion, as the vertical divergence of the density weighted momentum flux is a measure of the GWF. The 10-day moving average zonal GWF at ~90 km, derived for 2013, is presented in Fig. 5(b) (in blue). It can be seen that the GWF, as in the case of the zonal GW momentum flux, is highly variable. Again, however, a seasonal cycle is clearly present. During January and February, the GWF is generally westward with a minimum of $-240 \pm 70\ m\ s^{-1}\ day^{-1}$ toward the end of January, with the exception of an eastward peak during early January. This perturbation, coincident with the January 2013 major SSW, is discussed in a related paper (de Wit et al., 2014). Around April the GWF turns eastward, and GWF remains predominantly eastward until mid-September, with peak values of $+380 \pm 70\ m\ s^{-1}\ day^{-1}$. From October onwards, GWF is again observed to be mainly westward.

Although the reported peak GWFs might appear high, monthly mean values are not inconsistent with theoretical considerations (Holton, 1983; Holton and Zhu, 1984) and previous observations. Hocking (2005) reported monthly average values of $200\ m\ s^{-1}\ day^{-1}$ derived from meteor radar observations in July and August at a northern hemisphere polar site. Considering the high variability in GWF observed in the 10-day moving averages shown in Fig. 5(b), it is not surprising that the monthly mean GWF for July and August is actually lower than this value (around $+100\ m\ s^{-1}\ day^{-1}$, not shown).

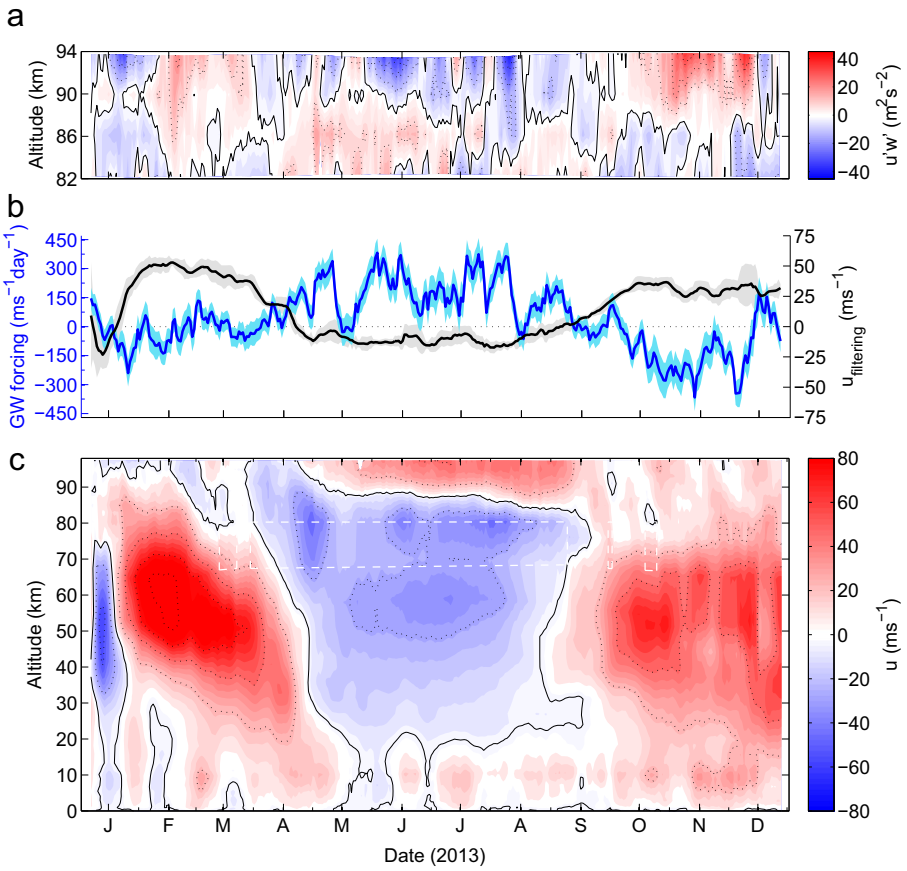

Fig. 5. (a) 10-day moving average zonal GW momentum flux $\overline{u'w'}$. ±10, 20 and 30 $m^2\ s^{-2}$, and zero contour are indicated by black dashed and solid lines, respectively. (b) 10-day moving average GW forcing (GWF, blue, left axis, uncertainty shaded) at ~90 km. The 10-day moving average net zonal wind between the surface and 80.5 km (black, right axis) is included as well (see Discussion section for details). (c) 10-day moving average zonal wind over Trondheim, using meteor radar observations (70–100 km) complemented with UKMO reanalysis results (below ~65 km). ±25, 50, 75 and 100 ms^{-1}, and zero contour are indicated by black dashed and solid lines, respectively. Areas inside white dashed line indicate regions during which no meteor radar winds could be derived, and results have been linearly interpolated in height.

The observed seasonal cycle in GWF, with generally eastward forcing in winter and westward forcing in summer, can be interpreted in terms of selective filtering of a uniform spectrum of upward propagating GWs in the underlying stratospheric wind field (e.g. Lindzen, 1981; Holton, 1983). To study the relation between the background wind profile and the GW momentum flux and forcing, the 10-day moving average time series of the zonal wind over Trondheim is shown in Fig. 5(c). In Fig. 5(c), the meteor radar wind data have been complemented by UK Met Office (UKMO) reanalysis results (Swinbank et al., 2013) for 63°N and 10°E below 70 km in order to study the zonal wind behavior over the full vertical range of the neutral atmosphere, from the surface to 100 km. Daily UKMO results are available at 12 UT, of which 10-day moving averages (time-stepped by 1 day) have been created.

From Fig. 5(c) it can be seen that eastward winds prevail over Trondheim in wintertime, except during early January when westward winds were present in response to a major SSW. Hence, during wintertime, filtering of eastward GWs in the wintertime polar vortex is expected to lead to a net westward GW momentum flux above the filtering region (Lindzen, 1981). When looking at the GW momentum flux at 82 km (Fig. 5(a)), it can be seen that in general westward GW momentum flux is indeed observed in winter.

As GWs propagate upward, their amplitudes continue to grow due to the decrease of density with height. Subsequent instability-driven GW breaking leads to the net deposition of westward momentum (or a westward GWF), and thus a removal of the westward waves from the flow. This behavior is most clearly illustrated in October and November in Fig. 5(a), when $\overline{u'w'}$ is seen to change from westward at 82 km to eastward above around 86 km. This, in turn, acts as a westward drag force on the eastward winds, reducing the eastward stratospheric jet. Indeed, it is not only the observed GWF that is westward at these times (Fig. 5(b)), but also the zonal wind exhibits a westward shear, leading to weaker eastward winds in the MLT than at around 60 km.

During summer, when westward winds are present throughout the middle atmosphere below the mesopause region (see Fig. 5 (c)), the reverse process occurs. Indeed, $\overline{u'w'}$ is seen to be generally eastward at 82 km in Fig. 5(a), and decreases with height to generate the eastward GWF observed in summer as seen in Fig. 5(b). Coincident with the period of eastward GWF, MLT zonal winds show an eastward shear, leading to eastward winds above about 85 km.

Upon closer inspection, it appears that the descent of the zero-wind line from May until about mid-August (Fig. 5(c)) is accompanied by a decrease in the altitude at which the GW momentum flux reverses from eastward to westward (Fig. 5(a)). This behavior has previously been noted by Placke et al. (2011a). This can again be interpreted as the interaction between GWs and zonal wind, in which upward propagation of eastward GWs is blocked by the eastward zonal winds encountered at the top of the domain, forcing GW breaking and deposition of eastward momentum (Placke et al., 2011a). Eastward momentum deposition imposes an eastward forcing in the region of the zero-wind line, speeding up the eastward winds above and slowing down the westward

winds below, resulting in the zero-wind line descending with time as seen in Fig. 5(c).

To study the relation between GWF and selective filtering of upward propagating GWs by the zonal wind field below the MLT in more detail, an estimate of the net zonal wind experienced by a symmetric distribution of upward propagating GWs centered around zero is shown in Fig. 5(b) (in black), together with the GWF (in blue). Here, the net zonal wind has been defined as the average of the most positive and most negative zonal wind in the vertical wind column between the surface and 80.5 km, giving an estimate of the asymmetry of the wind field underlying the region used in the determination of the GWF. This asymmetry is a measure for the opacity of the wind profile to upward propagating GWs (de Wit et al., 2013).

As can be seen from Fig. 5(b), from May until mid-September the net zonal wind is westward and GWF during these times is eastward, in agreement with the filtering of westward GWs by the underlying westward winds. From mid-September until the end of the year the opposite is true, with eastward net zonal wind generally coinciding with westward GWF. From mid-January until mid-April eastward net zonal winds are present, during which the GWF is generally westward or not statistically significantly different from zero.

From Fig. 5(b), it appears that the net zonal wind and GWF are negatively correlated, in accordance with the behavior expected from selective filtering arguments. Calculation of the zero-lag correlation between the net zonal wind and the GWF supports this notion. Both variables are significantly correlated above the 99% confidence level, with a correlation coefficient of -0.66. By considering the GWF as a function of the net zonal wind below the mesopause, the effect of changes in the zonal wind field on GWF can be estimated using a linear least-squares fit. It is found that each 1 m s^{-1} increase in net zonal wind leads to a decrease in mesopause region GWF of 4.6 ± 0.3 m s^{-1} day^{-1}.

From the above discussion it appears that on seasonal time scales the observed GWF can be interpreted by selective filtering of a symmetric distribution of upward propagating GWs originating from the lower atmosphere by the zonal wind field below the mesopause. This results in the observed westward forcing in winter and eastward forcing in summer. Furthermore, the strength of the net zonal wind below the mesopause can be used as a quantitative proxy for the magnitude and direction of the GWF in the MLT on seasonal time scales. On shorter time scales, however, the strong temporal variability as seen in the GWF, which is not present in the net zonal wind, suggests that in addition to selective filtering of vertically propagating GWs other processes play a role in the determination of GWF on shorter time scales. These processes could include temporal variability in GW generation, for example over the Scandinavian mountain range; the influence of the background zonal wind in the mesopause region on wave breaking (Andrews et al., 1987); or the secondary generation of GWs in the stratosphere, for example due to their dependence on the edge of the polar vortex (e.g. Satomura and Sato, 1999; Sato and Yoshiki, 2008).

5. Outlook and summary

A new generation SKiYMET meteor radar, optimized to derive high-frequency GW momentum flux, was installed in Trondheim, Norway (63.4°N, 10.5°E) and has been operational since September 2012. In addition to high-frequency GW momentum fluxes, high resolution zonal and meridional wind as well as daily temperature estimates can be derived (Hocking et al., 2001). Its location, at the edge of the polar vortex, is particularly well suited to study GW momentum flux variability related to disturbed and undisturbed vortex conditions. In addition, the presence of the quiet time auroral oval just north of the station enables future studies related to ionospheric disturbances. Together with the meteor radars located in Andenes, Norway (69°N, 16°E) (Singer et al., 2004) and Esrange, Sweden (68°N, 21°E) (Mitchell et al., 2002) the Trondheim radar creates a triangle over the Scandinavian mountain range, allowing for example studies of the influence of the mountain range on the MLT wind field. The current study presented the first observations of the seasonal cycle of high frequency GW momentum flux and forcing during 2013 obtained with the Trondheim meteor radar.

The system is optimized to measure high-frequency GW momentum fluxes with an 8 antenna transmitter array, steering most of the energy in the 15–50° zenith angle region. The system's 30 kW peak power leads to daily unambiguous meteor detection rates of between 5000 and 7000 in winter and up to 12 000 in summer in the altitude region between 70 and 100 km and over zenith angles between 15 and 50°. Meteor detections were found to maximize around 90 km, and are generally high enough to routinely determine winds between 75 and 100 km in winter and 80 and 100 km in summer. A daily cycle in meteor count rate as well as azimuth angle has been quantified.

Monthly mean values of the vertical flux of zonal and meridional momentum for March, June, September and December were presented for the Trondheim MLT. The meridional momentum flux, $\overline{v'w'}$, was found to range between ± 10 m^2 s^{-2}, while values for the zonal momentum flux, $\overline{u'w'}$, were found to be between -20 and $+10$ m^2 s^{-2}. Both components were found to be of the same order of magnitude as previous GW momentum flux observations.

Studying the 10-day moving average of $\overline{u'w'}$ shows generally a change from westward to eastward with height in winter, and from eastward to westward in summer. This vertical gradient leads to the observed seasonal cycle in GWF, with westward forcing in winter, and eastward forcing in summer. The seasonal cycle in both $\overline{u'w'}$ and GWF can be interpreted in terms of selective filtering of a uniform spectrum of vertically propagating GWs between the surface and the mesopause. In addition it was shown that the asymmetry in the wind field underlying the mesopause region can be used as a simple yet quantitative proxy for the seasonal variability of GWF in the mesopause.

Acknowledgements

This study was partly supported by the Research Council of Norway/CoE under Contract 223252/F50. The authors acknowledge the use of UK Met Office Stratospheric Assimilated Data, available from http://badc.nerc.ac.uk/browse/badc/ukmo-assim/. We thank the staff of Genesis Software for the installation and support of the radar, and Wayne Hocking for helpful discussions.

References

Andrews, D.G., Holton, J.R., Leovy, C.B., 1987. Middle Atmosphere Dynamics. Academic Press, London, UK.

Andrioli, V.F., Fritts, D.C., Batista, P.P., Clemesha, B.R., 2013. Improved analysis of all-sky meteor radar measurements of gravity wave variances and momentum fluxes. Ann. Geophys. 31 (5), 889–908. http://dx.doi.org/10.5194/angeo-31-889-2013.

Antonita, T.M., Ramkumar, G., Kumar, K.K., Deepa, V., 2008. Meteor wind radar observations of gravity wave momentum fluxes and their forcing toward the mesospheric semiannual oscillation. J. Geophys. Res. 113 (D10), http://dx.doi.org/10.1029/2007JD009089.

Becker, E., 2009. Sensitivity of the upper mesosphere to the Lorenz energy cycle of the troposphere. J. Atmos. Sci. 66 (3), 647–666. http://dx.doi.org/10.1175/2008JAS2735.1.

de Wit, R.J., Hibbins, R.E., Espy, P.J., Mitchell, N.J., 2013. Interannual variability of mesopause zonal winds over ascension Island: coupling to the stratospheric QBO. J. Geophys. Res. Atmos. 118 (21), 12052–12060. http://dx.doi.org/10.1002/2013JD020203.

de Wit, R.J., Hibbins, R.E., Espy, P.J., Orsolini, Y.J., Limpasuvan, V., Kinnison, D.E., 2014. Observations of gravity wave forcing of the mesopause region during the January 2013 major Sudden Stratospheric Warming. Geophys. Res. Lett. 41, http://dx.doi.org/10.1002/2014GL060501.

Ern, M., Preusse, P., Gille, J.C., Hepplewhite, C.L., Mlynczak, M.G., Russell III, J.M., Riese, M., 2011. Implications for atmospheric dynamics derived from global observations of gravity wave momentum flux in stratosphere and mesosphere. J. Geophys. Res. 116 (D19107), http://dx.doi.org/10.1029/2011JD015821.

Espy, P.J., Hibbins, R.E., Swenson, G.R., Tang, J., Taylor, M.J., Riggin, D.M., Fritts, D.C., 2006. Regional variations of mesospheric gravity-wave momentum flux over Antarctica. Ann. Geophys. 24, 81–88. http://dx.doi.org/10.5194/angeo-24-81-2006.

Espy, P.J., Jones, G.O.L., Swenson, G.R., Tang, J., Taylor, M.J., 2004. Seasonal variations of the gravity wave momentum flux in the Antarctic mesosphere and lower thermosphere. J. Geophys. Res. 109 (D23109), http://dx.doi.org/10.1029/2003JD004446.

Fleming, E., Chandra, S., Barnett, J., Corney, M., 1990. Zonal mean temperature, pressure, zonal wind, and geopotential height as functions of latitude, COSPAR international reference atmosphere: 1986, Part II: middle atmosphere models. Adv. Space Res. 10 (12), 11–59.

Fritts, D.C., Alexander, M.J., 2003. Gravity wave dynamics and effects in the middle atmosphere. Rev. Geophys. 41 (1), 1003. http://dx.doi.org/10.1029/2001RG000106.

Fritts, D.C., Janches, D., Hocking, W.K., 2010a. Southern Argentina Agile meteor radar: initial assessment of gravity wave momentum fluxes. J. Geophys. Res. 115 (D19123), http://dx.doi.org/10.1029/2010JD013891.

Fritts, D.C., Janches, D., Iimura, H., Hocking, W.K., Mitchell, N.J., Stockwell, R.G., Fuller, B., Vandepeer, B., Hormaechea, J., Brunini, C., Levato, H., 2010b. Southern Argentina agile meteor radar: system design and initial measurements of large-scale winds and tides. J. Geophys. Res. 115 (D18112), http://dx.doi.org/10.1029/2010JD013850.

Fritts, D.C., Vincent, R.A., 1987. Mesospheric momentum flux studies at Adelaide, Australia: observations and a gravity wave-tidal interaction-model. J. Atmos. Sci. 44 (3), 605–619. http://dx.doi.org/10.1175/1520-0469(1987)044⟨0605:MMFSAA⟩2.0.CO;2.

Fritts, D.C., Janches, D., Iimura, H., Hocking, W.K., Bageston, J.V., Leme, N.M.P., 2012. Drake Antarctic Agile Meteor Radar first results: configuration and comparison of mean and tidal wind and gravity wave momentum flux measurements with Southern Argentina agile meteor radar. J. Geophys. Res. 117 (D02105), http://dx.doi.org/10.1111/j.1747-1567.2010.00671.x.

Fritts, D.C., Janches, D., Riggin, D.M., Stockwell, R.G., Sulzer, M.P., Gonzalez, S., 2006. Gravity waves and momentum fluxes in the mesosphere and lower thermosphere using 430 MHz dual-beam measurements at Arecibo: 2. Frequency spectra, momentum fluxes, and variability. J. Geophys. Res. 111 (D18108), http://dx.doi.org/10.1029/2005JD006883.

Gardner, C.S., Gulati, K., Zhao, Y., Swenson, G., 1999. Measuring gravity wave momentum fluxes with airglow imagers. J. Geophys. Res. 104 (D10), 11903–11915. http://dx.doi.org/10.1029/1999JD900105.

Geller, M.A., Alexander, M.J., Love, P.T., Bacmeister, J., Ern, M., Hertzog, A., Manzini, E., Preusse, P., Sato, K., Scaife, A.A., Zhou, T., 2013. A comparison between gravity wave momentum fluxes in observations and climate models. J. Clim. 26 (17), 6383–6405. http://dx.doi.org/10.1175/JCLI-D-12-00545.1.

Hocking, W.K., 2005. A new approach to momentum flux determinations using SKiYMET meteor radars. Ann. Geophys. 23 (7), 2433–2439. http://dx.doi.org/10.5194/angeo-23-2433-2005.

Hocking, W.K., Fuller, B., Vandepeer, B., 2001. Real-time determination of meteor-related parameters utilizing modem digital technology. J. Atmos. Sol. Terr. Phys. 63 (2-3), 155–169. http://dx.doi.org/10.1016/S1364-6826(00)00138-3.

Hocking, W.K., 2011. A review of mesosphere–stratosphere–troposphere (MST) radar developments and studies circa 1997–2008. J. Atmos. Sol. Terr. Phys. 73 (9), 848–882. http://dx.doi.org/10.1016/j.jastp.2010.12.009.

Holton, J.R., 1983. The influence of gravity wave breaking on the general circulation of the middle atmosphere. J. Atmos. Sci. 40, 2497–2507. http://dx.doi.org/10.1175/1520-0469(1983)040⟨2497:TIOGWB⟩2.0.CO;2.

Holton, J.R., Zhu, X., 1984. A further study of gravity wave induced drag and diffusion in the mesosphere. J. Atmos. Sci. 41 (18), 2653–2662. http://dx.doi.org/10.1175/1520-0469(1984)041⟨2653:AFSOGW⟩2.0.CO;2.

Janches, D., Fritts, D.C., Riggin, D.M., Sulzer, M.P., Gonzalez, S., 2006. Gravity waves and momentum fluxes in the mesosphere and lower thermosphere using 430 MHz dual-beam measurements at Arecibo: 1. Measurements, methods, and gravity waves. J. Geophys. Res. 111 (D18107), 20. http://dx.doi.org/10.1029/2005JD006882.

Kleinknecht, N.H., Espy, P.J., Hibbins, R.E., 2014. The climatology of zonal wave numbers 1 and 2 planetary wave structure in the MLT using a chain of Northern Hemisphere SuperDARN Radars. J. Geophys. Res. Atmos. 119, 1292–1307. http://dx.doi.org/10.1002/2013JD019850.

Lindzen, R.S., 1981. Turbulence and stress owing to gravity-wave and tidal breakdown. J. Geophys. Res. 86 (C10), 9707–9714. http://dx.doi.org/10.1029/JC086iC10p09707.

Mitchell, N., Pancheva, D., Middleton, H., Hagan, M., 2002. Mean winds and tides in the arctic mesosphere and lower thermosphere. J. Geophys. Res. 107 (A1), 1004. http://dx.doi.org/10.1029/2001JA900127.

Nappo, C., 2002. An Introduction to Atmospheric Gravity Waves. Elsevier Academic Press, San Diego, CA, USA.

Pancheva, D.V., Mitchell, N.J., 2004. Planetary waves and variability of the semidiurnal tide in the mesosphere and lower thermosphere over Esrange (68°N, 21°E) during winter. J. Geophys. Res. 109 (A08307), http://dx.doi.org/10.1029/2004JA010433.

Placke, M., Hoffmann, P., Becker, E., Jacobi, C., Singer, W., Rapp, M., 2011a. Gravity wave momentum fluxes in the MLT—Part II: meteor radar investigations at high and midlatitudes in comparison with modeling studies. J. Atmos. Sol. Terr. Phys. 73 (9), 911–920. http://dx.doi.org/10.1016/j.jastp.2010.05.007.

Placke, M., Stober, G., Jacobi, C., 2011b. Gravity wave momentum fluxes in the MLT—Part I: seasonal variation at Collm 5.13°N, 1.30°E. J. Atmos. Sol. Terr. Phys. 73 (9), 904–910. http://dx.doi.org/10.1016/j.jastp.2010.07.012.

Reid, I.M., Vincent, R.A., 1987. Measurements of mesospheric gravity-wave momentum fluxes and mean flow accelerations at adelaide, Australia. J. Atmos. Terr. Phys. 49 (5), 443–460. http://dx.doi.org/10.1016/0021-9169(87)90039-0.

Sandford, D.J., Beldon, C.L., Hibbins, R.E., Mitchell, N.J., 2010. Dynamics of the Antarctic and Arctic mesosphere and lower thermosphere—Part 1: mean winds. Atmos. Chem. Phys. 10, 10273–10289. http://dx.doi.org/10.5194/acp-10-10273-2010.

Sato, K.M., Yoshiki, M., 2008. Gravity wave generation around the polar vortex in the stratosphere revealed by 3-hourly radiosonde observations at Syowa station. J. Atmos. Sci. 65, 3719–3735. http://dx.doi.org/10.1175/2008JAS2539.1.

Satomura, T.K., Sato, K., 1999. Secondary generation of gravity waves associated with the breaking of mountain waves. J. Atmos. Sci. 56, 3847–3858. http://dx.doi.org/10.1175/1520-0469(1999)056⟨3847:SGOGWA⟩2.0.CO;2.

Singer, W., von Zahn, U., Weiß, J., 2004. Diurnal and annual variations of meteor rates at the Arctic circle. Atmos. Chem. Phys. 4, 1355–1363. http://dx.doi.org/10.5194/acp-4-1355-2004.

Stober, G., Jacobi, C., Matthias, V., Hoffmann, P., Gerding, M., 2012. Neutral air density variations during strong planetary wave activity in the mesopause region derived from meteor radar observations. J. Atmos. Sol. Terr. Phys. 74, 55–63. http://dx.doi.org/10.1016/j.jastp.2011.10.007.

Swinbank, R., O'Neill, A., Lorenc, A.C., Ballard, S.P., Bell, R.S., Ingleby, N.B., Andrews, P.L. F., Barker, D.M., Bray, J.R., Clayton, A.M., Dalby, T., Li, D., Payne, T.J., Saunders, F.W., Macpherson, B., Cullen, M.J.P., Davies, T., Mawson, M.H., 2013. Stratospheric Assimilated Data, [Internet]. NCAS British Atmospheric Data Centre, 2006 Available from ⟨http://badc.nerc.ac.uk/view/badc.nerc.ac.uk__ATOM__dataent_ASSIM⟩.

Tang, J., Liu, A.Z., Swenson, G.R., 2002. High frequency gravity waves observed in OH airglow at starfire optical range, NM: seasonal variations in momentum flux. Geophys. Res. Lett. 29 (20), http://dx.doi.org/10.1029/2002GL015794.

Vincent, R.A., Reid, I.M., 1983. HF Doppler measurements of mesospheric gravity wave momentum fluxes. J. Atmos. Sci. 40, 1321–1333 doi:10.1175/1520-0469(1983)040 1321:HDMOMG 2.0.CO;2.

Vincent, R.A., 2009. Gravity wave coupling from below: a review. In: Tsuda, T., Fujii, R., Shibata, K., Geller, M.A. (Eds.), Climate and Weather of the Sun–Earth System (CAWSES), Selected Papers from the 2007 Kyoto Symposium, 2009, pp. 279–293.

Younger, P.T., Astin, I., Sandford, D.J., Mitchell, N.J., 2009. The sporadic radiant and distribution of meteors in the atmosphere as observed by VHF radar at Arctic Antarctic, and equatorial latitudes. Ann. Geophys. 27, 2831–2841. http://dx.doi.org/10.5194/angeo-27-2831-2009.